Proceedings of the
Annual Stability Conference
Structural Stability Research Council
Louisville, Kentucky, April 1-4, 2025

Local buckling of extruded aluminum circular hollow sections under combined load cases

Moufahdilou Ouro-Yendou[1], Nicolas Boissonnade[2], Liya Li[3]

Abstract
This paper investigates the local buckling behavior of extruded aluminum circular hollow sections (CHS) under combined compression and bending loads. Based on non-linear shell Finite Element (F.E.) models validated against experimental tests, systematic numerical analyses were conducted to explore the performance of aluminum CHS members as influenced by local buckling and stress distributions. The F.E. studies study considered a wide range of parameters, including cross-section dimensions, slenderness ratios and aluminum alloys. Additionally, various loading scenarios, including varying proportions of compression and bending, were analyzed to consider all possible structural conditions. The experimental and numerical results were compared with current design standards. The results revealed that current Canadian design standards tend to provide conservative design predictions for aluminum CHS under combined loading conditions, leading to uneconomical design solution. To address this, an advanced design method is proposed, which provides a more accurate and less conservative prediction of the load-bearing capacity of extruded aluminum CHS.

1. Introduction
In recent years, the global aluminum production sector has exploded in several fields including automobile construction, shipbuilding and aeronautics (Canada 2018). Civil engineering also benefits from the unique advantages of aluminum alloys. These include corrosion resistance, high strength-to-weight ratio, recyclability, improved performance at low temperatures (a significant advantage in Canada and Quebec's cold winters), and ease of manufacturing. Extrusion, for example, allows for creating diverse shapes and geometries. These features, along with others, make aluminum alloys an appealing choice in the field (Georgantzia, Gkantou, and Kamaris 2021). Engineers and researchers in civil engineering and construction are increasingly focusing on aluminum as a key structural material. Circular Hollow Sections (CHS) made from aluminum are particularly gaining attention for their versatility. They are widely used in structures such as road signs, pedestrian walkways, and lattice frameworks for bridges and footbridges. Aluminum CHS is also commonly employed in other roadside signage structures. Nevertheless, the extensive use of CHS faces challenges due to their buckling behavior. Hollow circular cross-section structures

[1] PhD Student, Sherbrooke University, <moufahdilou.ouro-yendou@usherbrooke.ca>
[2] Professor, Laval University, < nicolas.boissonnade@gci.ulaval.ca>
[3] Professor, Sherbrooke University, < liya.li@usherbrooke.ca>

show complex shell buckling behavior because of their three-dimensional constitution (S. Timoshenko, 1959) (Echeverri Loaiza et al. 2024), this complexity is further amplified by their sensitivity to geometric imperfections, especially in slender cross-sections. In contrast, hollow square cross-sections, composed of flat plates, buckle in a simpler two-dimensional manner (Stability of Structures 2010). It follows from this observation that current design standards are overly conservative for predicting the resistance of aluminum CHS as they fail to fully exploit the advantages of aluminum as a structural material (Georgantzia, Gkantou, and Kamaris 2021).

Therefore, with the aim of improving design standards, researchers such as Zhu and Young have carried out experimental tests on the bending and beam-column resistance of CHS made from 6061-T6 alloys (Zhu and Young 2006, 2008). After comparison with some design standards like the Eurocode 9 standard (EN1999 Eurocode 9 2001) and the ADM (Aluminum Design Manual 2020 | The Aluminum Association 2020), results showed that the latter were conservative and therefore did not really predict the actual strength of aluminum CHS. In addition, other researchers such as Rong and al., have carried out experimental and numerical studies on CHS subjected to eccentric loading, considering several parameters including the dimensions of the section, its slenderness and the amplitude of the overall imperfection (Rong et al. 2022). This latter study showed, after comparison with Eurocode 9 (EN1999 Eurocode 9 2001), that it was also conservative. In view of the above findings, Li and al. (Li et al. 2023) decided to carry out experimental investigations to study the ultimate capacities and failure modes of extruded CHS 6061-T6 aluminum alloy columns under axial and eccentric compression, taking account of the amplitude of local imperfections. In this study, the researchers were able to demonstrate the accuracy of a new dimensioning method based on the Overall Interaction Concept (O.I.C).

In this paper, the objective is to investigate the local buckling behavior of hollow circular aluminum sections (CHS) subjected to combined compressive and bending loading cases. To this end, Section 2 presents a brief overview of the Canadian design standard CSA S157 standard (CSA S157-17/S157.1-17 2022) and the O.I.C. concept, and their approach to predicting the resistive capacity of CHS. Then in Section 3, a finite element-based numerical model is develop using ABAQUS software. In section 4, a validation of the model is carried out based on results previously obtained from experimental tests carried out by Li and al., (Li et al. 2023) for short columns. Once all the validations have been carried out, Section 5 deals with the parametric study, including section dimensions, slenderness, alloy type, different load combinations and local imperfection amplitudes. Finaly the section 6 then analyzes the results of the parametric study, comparing them with the results of the CSA S157 and developing design rules based on the O.I.C.

2. Canadian Design Standards CSA S157 and Overall Interaction Concept (O.I.C.)

2.1 Canadian design rule for Simple and Combined loading cases

Aluminum structures are designed in accordance with CSA standard S157-17 (CSA S157-17/S157.1-17 2022) in Canada.

For CHS under axial compression as influenced by local buckling, the CSA S157 recommends applying the formula of Eq. 1 to determine the value of N_{r} which denotes the axial compressive strength of the CHS cross section.

$$N_{\mathrm{r}} = \phi_{\mathrm{y}} A_{\mathrm{g}} \bar{F} F_y \tag{1}$$

In this equation, ϕ_y represents the safety coefficient, A_g the value of the gross section, $\bar{F}$ the value of the normalized buckling stress and F_y represent yield strength. For determining the value of $\bar{F}$, CSA S157 provides in detail through Eq. 2 to 5 of this paper the appropriate detailed formulas.

$$\bar{F} = \beta - \sqrt{\beta^2 - \frac{1}{\bar{\lambda}^2}} \tag{2}$$

$$\text{Where} \quad \beta = \frac{1 + \alpha(\bar{\lambda} - \bar{\lambda}_0) + \bar{\lambda}^2}{2\bar{\lambda}^2} \tag{3}$$

$$\text{With} \quad \bar{\lambda} = \frac{\lambda}{\pi}\sqrt{\frac{F_y}{E}} \tag{4}$$

$$\text{And} \quad \lambda = 4\sqrt{\frac{R_{max}}{t}}\left(1 + 0.03\sqrt{\frac{R_{max}}{t}}\right) \tag{5}$$

In these formulas, $\bar{\lambda}$ represents the normalized section slenderness and $\bar{\lambda}_0$ equals to 0.5 for verifying cross-sectional resistance. Second, the α value considers the nature of the aluminum alloy, i.e. α takes either the value of 0.2 for heat-treated alloys (as in this paper) or the value of 0.4 for non-heat-treated alloys. F_y is the yield strength (0.2% proof stress) of the aluminum alloys, and E corresponds to its Young's modulus. In addition, R_{max} refers to the maximum radius of the CHS and t the wall thickness as shown in Fig. 1.

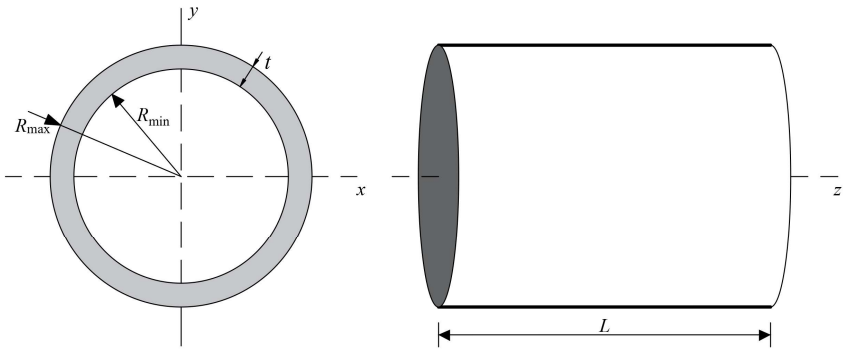

Figure 1: Representation of CHS dimensions in Cartesian coordinates

To evaluate the bending resistance of CHS, the CSA S157 applies classic cross-section classification concept like most of current dimensioning standards. Cross-sections are then subdivided into three groups according to the value of their cross-section slenderness $\bar{\lambda}$. Sections are divided into three categories. As illustrated in Fig. 1, class 1 sections are the most compact and can develop their full capacity and reach the plastic moment M_p. Class 2 sections are semi-compact sections and reach the elastic moment M_y. Class 3 sections may subject to local buckling before developing elastic moment M_y.

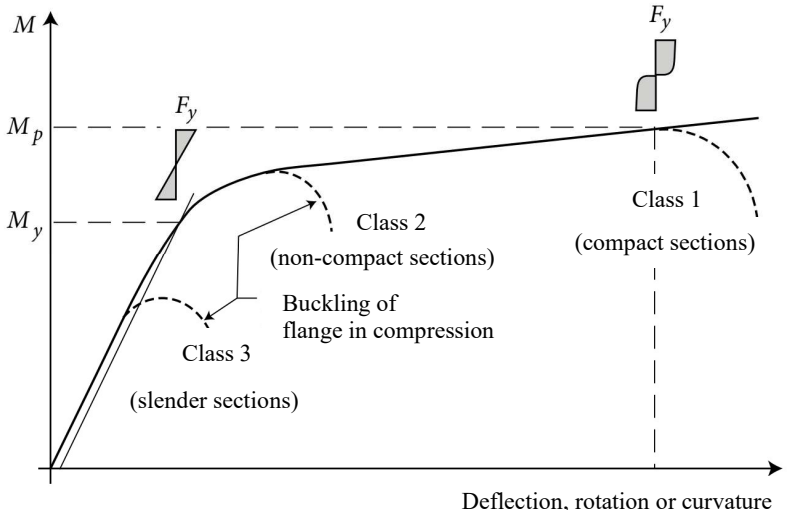

Figure 2: Failure by flange buckling due to bending (Beaulieu 2006)

According to CSA S157, it is the normalized slenderness $\bar{\lambda}$ that determines the section class, as determined in Eq. 6.

$$\begin{cases} \bar{\lambda} \leq \bar{\lambda}_0 = 0.3 \Rightarrow \text{Class 1} \\ \bar{\lambda} \leq \bar{\lambda}_0 = 0.5 \Rightarrow \text{Class 2} \\ \bar{\lambda} > \bar{\lambda}_0 = 0.5 \Rightarrow \text{Class 3} \end{cases} \tag{6}$$

Once the cross-sections have been classified, CSA S157 recommends proceeding to the calculation of the bending strength M_{f}. Eq. 7 presents the formulas for each type of section class. In this equation, Z designates the section's plastic modulus and S its elastic modulus.

$$\begin{cases} \text{Class 1: } M_{\mathrm{f}} = \phi_{\mathrm{y}} Z F_{\mathrm{y}} \\ \text{Class 2: } M_{\mathrm{f}} = \phi_{\mathrm{y}} S F_{\mathrm{y}} \\ \text{Class 3: } M_{\mathrm{f}} = \phi_{\mathrm{y}} S \bar{F} F_{\mathrm{y}} \end{cases} \tag{7}$$

After determining the resistive capacities of CHS under simple load cases, N_r (axial resistance) and M_r (moment resistance), the next step is to account for the interaction between compression and bending. The CSA S157 standard addresses this by applying an interactive equation to evaluate the combined effect of compression and bending resistances (see Eq. 8). In this equation, P_{f} represents the axial compressive force applied to the structure, P_{r} the axial resistance of the cross-section of the structure that the latter can support, M_{f} externals moments exerted on the element and M_{r} the resistance to bending that the cross-section of the structure can offer.

$$\frac{P_{\mathrm{f}}}{P_{\mathrm{r}}} + \frac{M_{\mathrm{f}}}{M_{\mathrm{r}}} \leq 1.0 \tag{8}$$

2.2 Overall Interaction Concept (O.I.C.) approach

As mentioned above, current design standards, including CSA S157, are too conservative to accurately predict actual CHS strengths. Therefore, new design methods like the Overall Interaction Concept (O.I.C.) approach have been developed. The O.I.C., which is based on the well-established resistance-instability interaction with a definition of generalized relative

slenderness, abandons the cross-section classification concept and calculates all cross-section shapes in a similar way for both sections and members, under simple or combined loading cases. Boissonnade et al. have illustrated the mechanical background of the O.I.C in (Boissonnade, Nseir, and Saloumi 2013). This approach emerged in recent few years ago through Nseir (Nseir 2015) and Hayeck (Hayeck 2016) respectively following their work on steel sections. the O.I.C. already applied to cross-sections and members. Later, researchers like Beyer (Beyer 2017) developed and extended the concept to U-sections subjected to combined loads (Li et al. 2022).

As shown in Fig. 3, the O.I.C. applies $\bar{\lambda}_L - \chi_L$ format (Li et al. 2023) describing the local buckling design curves. The $\bar{\lambda}_L$ is designated as the cross-section local relative slenderness that takes the balance between plastic resistance and the section's local instability (Dahboul et al. 2023) and χ_L is the cross-section local buckling factor (Li et al. 2022) that decreases the plastic capacity kept as a reference to account for the influences of buckling and imperfections (Dahboul et al. 2023) as illustrated on formulas on Fig. 3. Several parameters are considered in establishing this curve, in particular the amplitude of imperfections, cross-section dimensions, aluminum material parameters and the various CHS strengths considered in different states. In addition, $R_{cr,L}$ represents the load ratio that need be applied to the initial loading to reach the (local) critical state. R_{pl} is the load ratio required to scale the initial loading to the plastic capacity. Finally, $R_{b,L}$ is the factor by which the initial loading shall be multiplied to achieve the ultimate capacity of the cross-sections (Dahboul et al. 2023).

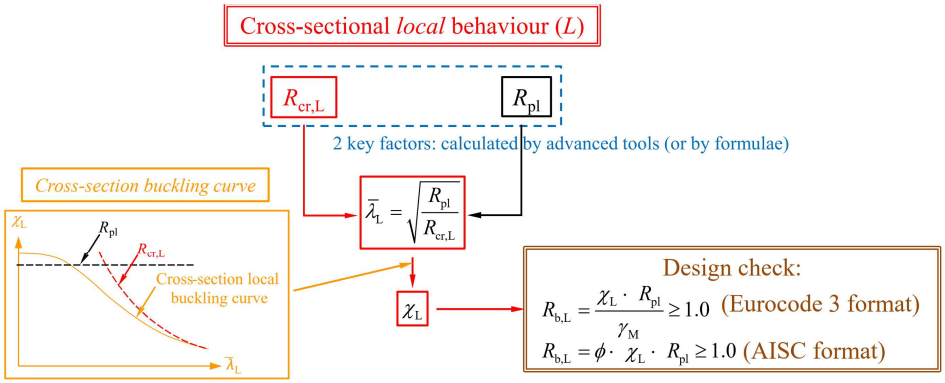

Figure 3: O.I.C. design flow chart for cross section resistance (Li et al. 2023)

Once all the *R*-factors have been calculated, the O.I.C. applies the Ayrton-Perry formulation to determine the buckling curves. In this equation, λ_0 is the slenderness value that defines the onset of local buckling observation, α_L the factor that drives the influence of imperfections on cross-sectional strength, and δ that manages the stability limit through post-buckling effects.

$$\chi_L = \frac{1}{\Phi_L + \sqrt{\Phi_L^2 - \bar{\lambda}_L^{\,\delta}}} \tag{9}$$

$$\text{Where} \quad \Phi_L = 0{,}5 \cdot (1 + \alpha_L \cdot (\bar{\lambda}_L - \lambda_0) + \bar{\lambda}_L^{\,\delta}) \tag{10}$$

This paper also addresses the case of combined compressive and bending loads. To account for these, the O.I.C. recommends initially calculating the effects of individual loads using $\chi_{N,L}$ and $\chi_{M,L}$. Once these values are determined, the O.I.C. defines a loading space in spherical coordinates. In this space, as illustrated in Fig. 4, each axis represents axial compression or bending along a specific axis. This framework allows the combined effects of compression and bending to be considered through proportions of these different loads, defined by the angle formed by $\chi_{L,combined}$ with the axes of the loading space (Dahboul et al. 2023). Eq. 11 provides the general formula for determining $\chi_{L,combined}$ for CHS - being symmetric in all aspects. In this equation, $\chi_{L,N}$ corresponds to the ordinates of the local buckling curve of the transverse section previously developed for compressive loads, while $\chi_{L,M}$ corresponds to those developed for bending loads. The parameters q_i are used to calibrate this combined curve.

$$\chi_{L,combined} = \left[(\chi_{L,N} \cdot \cos^{q_2}\theta)^{q_1} + (\chi_{L,M} \cdot \sin^{q_3}\theta)^{q_1}\right]^{\frac{1}{q_1}} \tag{11}$$

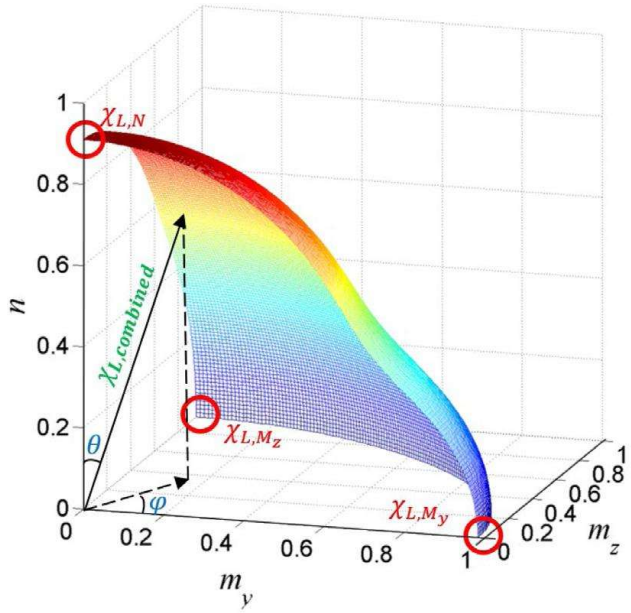

Figure 4: O.I.C 3D loading space (Li et al. 2022)

3. Numeric study

This paper makes non-linear analyses of Finite Element (F.E.) models of aluminum CHS to design the O.I.C. interaction curve. Numerical calculations are based on previously designed F.E. models that consider several key elements to reproduce realistic experimental test conditions. Once these models had been obtained, a validation of them is made, basis on experimental results obtained in the work of Li et al. (Li et al. 2023) for short column. That validation consists in comparing the experimental results with those obtained numerically through a GMNIA analysis (Geometrically and materially nonlinear analysis with imperfections).

3.1 Development of the F.E. numerical simulation models

F.E. models integrate several elements and concepts to obtain results very close to reality. For this purpose, S4R-type shell elements are used as the shape model, with a Risk method analysis to consider the non-linear behavior of cross-sections. About the mesh density size used, the work of Echeverri Loaiza et al. (Echeverri Loaiza et al. 2024) recommended to take the mesh dimension

equals to $0{,}1 \cdot \sqrt{D_{max} \cdot t}$ for each element. The local imperfection amplitude was selected as $\frac{t}{2000}\left(\frac{D_{max}}{t}\right)^{1,5}$ as recommended by (Echeverri Loaiza et al. 2024).s

$$\omega = \frac{t}{2000}\left(\frac{D_{max}}{t}\right)^{1,5} \; ; \; n = \begin{cases} 1 \\ 3 \\ 5 \end{cases} \tag{12}$$

As shown in Fig. 5, the local imperfections consist of a pattern of sinusoidal curves with a maximum amplitude at the center. Three different n values were chosen as the number of halfwaves, as mentioned in Eq. 12.

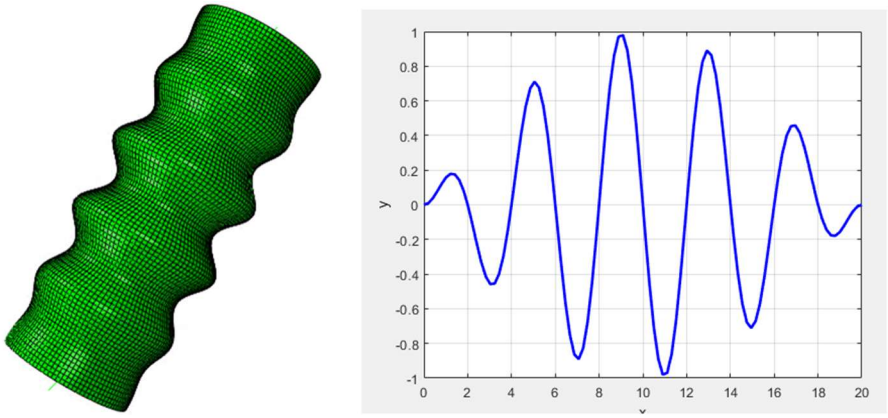

Figure 5: local imperfection with annealed mode pattern (Echeverri Loaiza et al. 2024)

For the validation of the numerical model, the boundary conditions of the Li et al. tests were reproduced in their entirety, to ensure that the results compared favourably with the experimental tests (Li et al. 2023). Li et al. 2023 tests were mainly based on compressive load applied on stub, short beam-column tests with an eccentricity or not. Fig. 6 shows the Boundary Conditions used in these two loading cases.

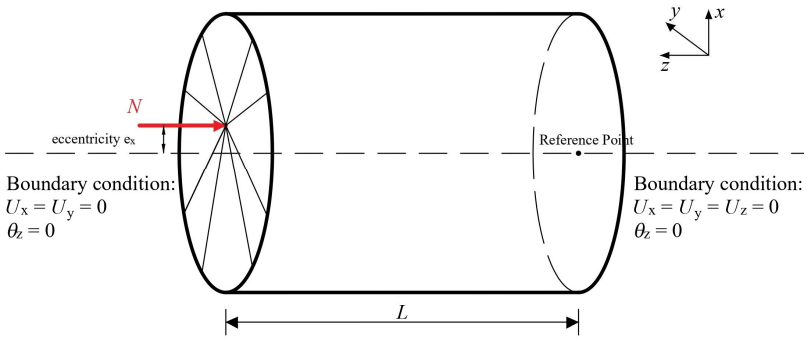

Figure 6: Boundary conditions used for validation test on stub, short beam-column CHS

In the case of the parametric study, boundary conditions were specified as shown in Fig. 7.

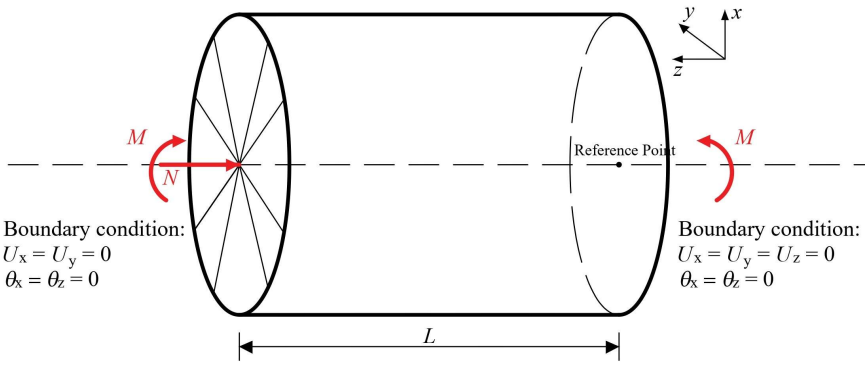

Figure 7: Boundary conditions used for parametric studies under combined load cases.

3.2 Validation of F.E. numerical simulation models

The numerical models were then validated with existing experimental test results (Li et al. 2023). All the measured parameters including section dimension, material properties, and loading eccentricities were incorporated into finite element (FE) models. Tables 1 and 2 present the validation results, where e represents the eccentricity of the applied compression load, $N_{\mathrm{u,exp}}$ denotes the experimental compression response, and $N_{\mathrm{u,FE}}$ corresponds to the numerical compression response. The accuracy of the validation results is expressed by using the ratio $\frac{N_{\mathrm{u,F.E.}}}{N_{\mathrm{u,Exp.}}}$. A ratio $\frac{N_{\mathrm{u,F.E.}}}{N_{\mathrm{u,Exp.}}} < 1$ indicates a conservative prediction, while $\frac{N_{\mathrm{u,F.E.}}}{N_{\mathrm{u,Exp.}}} > 1$ suggests an overestimated, potentially unsafe prediction.

Table 1: Geometric sections tested for Compression validation on shorts CHS (Li et al. 2023)

Specimen	E [MPa]	F_y [MPa]	D_{max} [mm]	t [mm]	L [mm]	e [mm]
Sc-A-1	69045	234	152.18	4.85	399.43	-
Sc-A-2			152.05	4.84	399.01	-
Sc-B-1	65549	276	202.67	3.24	598.67	-
Sc-B-2			202.56	3.26	598.82	-
Sbc-A-e1-1	69045	234	152.06	4.85	399.64	10.32
Sbc-A-e1-2			152.12	4.86	399.75	14.27
Sbc-A-e2-1			152.11	4.82	448.79	59.28
Sbc-A-e2-2			152.08	4.87	399.74	55.59
Sbc-A-e3-1			152.10	4.88	398.88	94.40
Sbc-A-e3-2			152.15	4.89	399.45	92.40
Sbc-B-e4-1	65549	276	202.90	3.19	598.34	27.50
Sbc-B-e4-2			202.96	3.20	598.70	29.12
Sbc-B-e5-1			202.90	3.25	598.37	43.45
Sbc-B-e5-2			202.96	3.20	598.82	42.60
Sbc-B-e6-1			202.54	3.45	598.95	59.72
Sbc-B-e6-2			202.54	3.45	599.00	56.03

Fig. 9 presents the results obtained from F.E. simulations, comparing the key parameters outlined in Eq. 13. Additionally, Figure 8 provides a detailed representation of the F.E. model, showcasing three distinct half-waves with exaggerated features for better visualization.

Table 2 and Fig. 9 summarize the essential numerical results for model validation, providing a comprehensive overview of the study's outcomes.

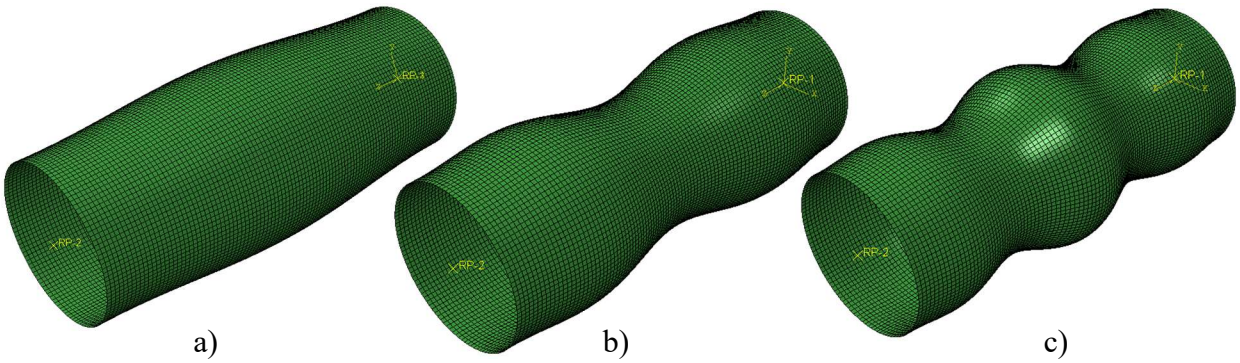

a) b) c)

Figure 8: F.E. model with n halfwaves: a) n = 1 – b) n = 3 – c) n = 5

Table 2: F.E. results for validation on Shorts CHS

Specimen	$N_{u,Exp.}$ [kN]	$N_{u,F.E.}/N_{u,Exp.}$ $n = 1$[1] [-]	$N_{u,F.E.}/N_{u,Exp.}$ $n = 3$ [-]	$N_{u,F.E.}/N_{u,Exp.}$ $n = 5$ [-]
Sc-A-1	576.65	0.97	0.97	0.94
Sc-A-2	540.38	1.03	1.03	1.00
Sc-B-1	481.68	1.14	1.13	1.11
Sc-B-2	489.05	1.13	1.12	1.10
Sbc-A-e1-1	443.09	1.08	1.08	1.05
Sbc-A-e1-2	425.23	1.08	1.07	1.04
Sbc-A-e2-1	232.60	1.22	1.21	1.20
Sbc-A-e2-2	259.88	1.16	1.15	1.11
Sbc-A-e3-1	202.34	1.09	1.08	1.05
Sbc-A-e3-2	182.88	1.22	1.22	1.19
Sbc-B-e4-1	364.48	1.08	1.07	1.02
Sbc-B-e4-2	375.52	1.04	1.03	0.98
Sbc-B-e5-1	325.39	1.06	1.04	0.99
Sbc-B-e5-2	314.45	1.06	1.07	1.01
Sbc-B-e6-1	270.18	1.19	1.19	1.09
Sbc-B-e6-2	281.76	1.18	1.18	1.10
	Mean	1.11	1.10	1.06
	C.OV.	0.07	0.07	0.07

1. n is the number of halfwaves

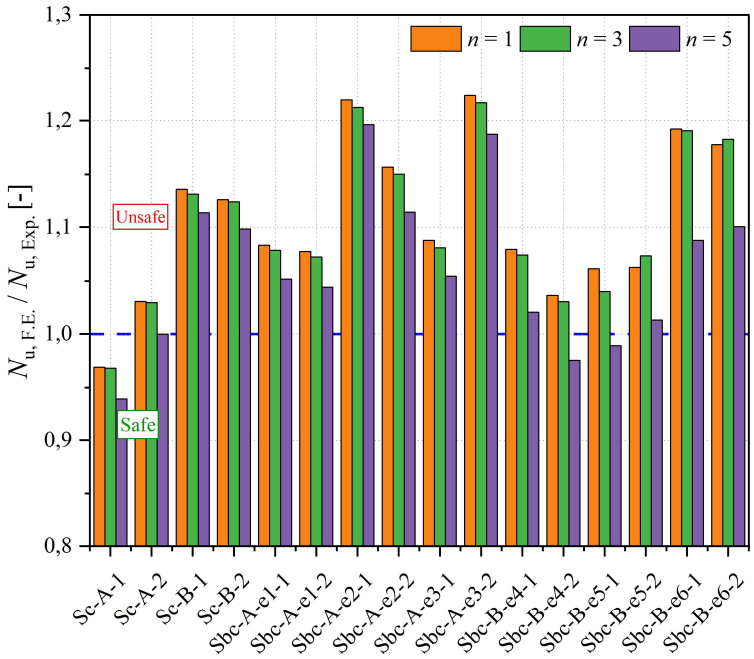

Figure 9: Comparison of experiments tests and F.E. results with different number of halfwaves for Short CHS

The validation results show that the model can adequately predict CHS resistance by maintaining a good coefficient of variation (COV) of 0.07 for any value of n. Nevertheless, for $n = 5$, the mean of the results is better and is 1.06. This number of halfwaves is therefore retained.

3.3 Parametric study

Validation of the model were used to have key parameters to perform the numerical models. For cross-section dimension, the D is between 21 mm and 118 mm, D/t is between 10 to 160 Three alloys were considered 6061-T6 with $F_y = 170$ MPa, 6061-T6 with $F_y = 240$ MPa and 6082-T6 with $F_y = 260$ MPa as they are frequently applied in civil engineering. The length of models L were selected as 3×D to balance between the edge effect in the end of sections and influence of global buckling

In these parametric studies, both simple load cases (N or M) and combined load cases ($N + M$) were considered. These load cases are derived from a loading surface governed by polar coordinates. As shown in Fig. 10, the horizontal axis represents the nominal bending resistance, mmm, while the vertical axis represents the nominal compression resistance, both normalized relative to the plastic resistance of the cross-section as a reference (see Eq. 16). In this equation, N_{r} and M_{r} represent the loads applied to the CHS during the numerical test, then N_{pl} and M_{pl} are the plastic loads associated with compression and bending respectively. The angle of variation θ varies between 0 and 90° with an iteration step of 15°. 90° correspond to pure bending m and 0° to pure compression. With the increase of θ, the participate of compression force is reduced with the increase of bending moment participation.

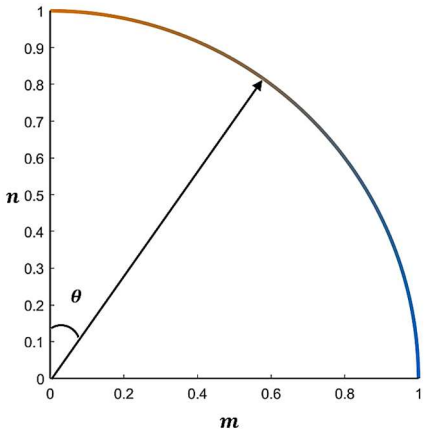

Figure 10: 2-dimensional $n - m$ loading space

$$n = \frac{N_r}{N_{\text{pl}}} = \frac{N_r}{A \cdot f_y} \quad ; \quad m = \frac{M_r}{M_{\text{pl}}} = \frac{M_{\text{r}}}{W_{\text{pl}} \cdot f_y} \tag{13}$$

$$\tan\theta = \frac{m}{n} = \frac{M_{\text{r}} \cdot A}{W_{\text{pl}} \cdot N_r} \tag{14}$$

$$\frac{N_r}{M_{\text{r}}} = \frac{A}{W_{\text{pl}} \cdot \tan\theta} \tag{15}$$

In total, 441 different cases were analysed. Note that ABAQUS was used to obtain the values of R_{cr} through Linear Buckling Analysis (LBA), R_{pl} through Material Non-linear Analysis (MNA), and $R_{b,L}$ through Generalized Material and Geometric Non-linear Analysis (GMNIA).

4. O.I.C proposal curve and comparison with CSA S157

The OIC design equations were then developed based on the numerical results as shown in Table 3.

Table 3: O.I.C. Design proposal for aluminum cross section under simple load cases and combined load cases

Load Cases		Compression N	Bending M
N or M		For $\bar{\lambda}_{L,N} \le \lambda_0 = 0.4$:	For $\bar{\lambda}_{L,M_z} \le \lambda_0 = 0.3$:
	Alloy 6063-T6	$\chi_{L,N} = -1.18\,\bar{\lambda}_{L,N} + 1.47$	$\chi_{L,M} = -1.4\,\bar{\lambda}_{L,M_z} + 1.42$
	Alloy 6061-T6	$\chi_{L,N} = -0.5\,\bar{\lambda}_{L,N} + 1.2$	$\chi_{L,M} = -0.7\,\bar{\lambda}_{L,M_z} + 1.21$
	Alloy 6082-T6	$\chi_{L,N} = -1.4\,\bar{\lambda}_{L,N} + 1.5$	$\chi_{L,M} = -1.6\,\bar{\lambda}_{L,M_z} + 1.48$
	Ayrton-Perry format	For $\bar{\lambda}_{L,N} > \lambda_0 = 0.4$:	For $\bar{\lambda}_{L,M_z} > \lambda_0 = 0.3$:
		$\Phi_L = 0{,}5 \cdot (1 + \alpha_L \cdot (\bar{\lambda}_{L,N} - \lambda_0) + \bar{\lambda}_{L,N}{}^{\delta})$	$\Phi_L = 0{,}5 \cdot (1 + \alpha_L \cdot (\bar{\lambda}_{L,M_z} - \lambda_0) + \bar{\lambda}_{L,M_z}{}^{\delta})$
		$\chi_{L,N} = \dfrac{1}{\Phi_L + \sqrt{\Phi_L^2 - \bar{\lambda}_{L,N}{}^{\delta}}}$	$\chi_{L,M} = \dfrac{1}{\Phi_L + \sqrt{\Phi_L^2 - \bar{\lambda}_{L,M_z}{}^{\delta}}}$
		$\alpha_L = 0.2$ and $\delta = 4$	$\alpha_L = 0.35$ and $\delta = 1.7$
$N + M$		$\chi_{L,combined} = \left[(\chi_{L,N} \cdot \cos^{7.5}\theta)^{9.5} + (\chi_{L,M} \cdot \sin^{0.06}\theta)^{9.5}\right]^{\frac{1}{9.5}}$	

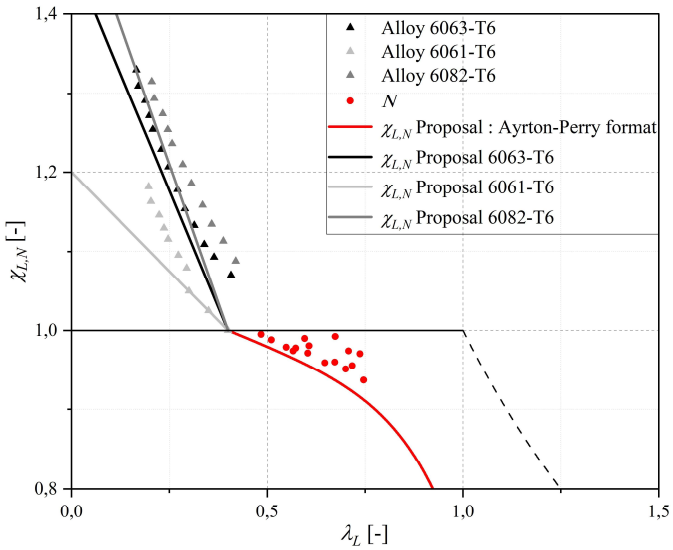

Figure 11: O.I.C proposal curve for pure compression (N) cases

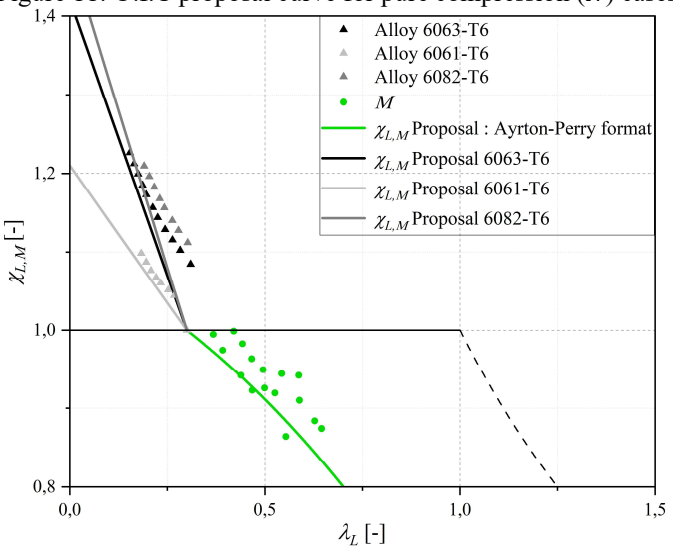

Figure 12: O.I.C proposal curve for pure bending (M) cases

As shown in Table 3, for cases of pure compression and pure bending, the O.I.C. curve is divided into two distinct regions. The first region, where $\bar{\lambda}_{L,N} < \lambda_0$, corresponds to the increase in resistance due to strain hardening, which depends on the alloy type. Different design curves were developed to account for variations among alloys. In the second region, where $\bar{\lambda}_{L,N} > \lambda_0$, a single design curve was applied to these cross-sections, reflecting the influence of local buckling. Figures 11 and 12 illustrate the comparison between the O.I.C. design curves and the corresponding numerical results for N and M, respectively

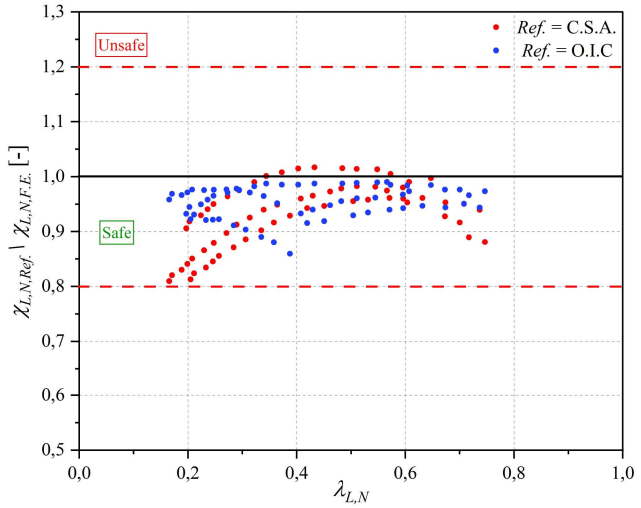

Figure 13: Comparison of O.I.C. and CSA S157 results with F.E. for N cases

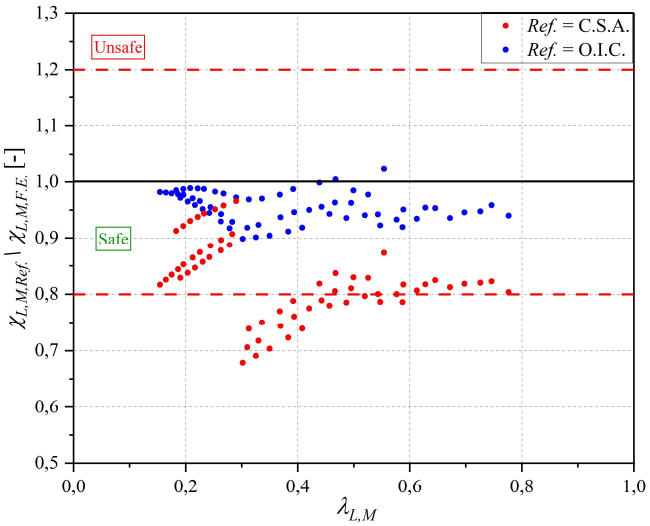

Figure 14: Comparison of O.I.C. and CSA S157 results with F.E. for M cases

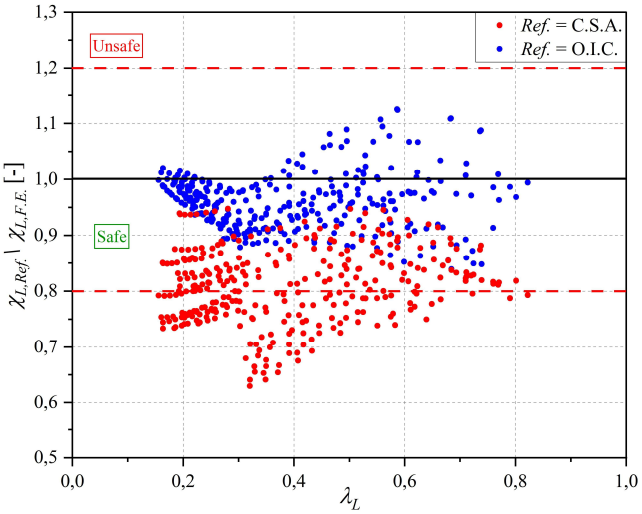

Figure 15: Comparison of O.I.C. and CSA S157 results with F.E. for $N + M$ cases

All the numerical results were compared with the CSA S157 and the O.I.C. proposal as illustrated on Fig.13 to Fig. 15. It was found that the results by the CSA S157, are conservative compared to those obtained for the O.I.C. for the most part. In addition, for medium slender sections, in the case of CSA S157 especially concerning bending and combine load cases for alloys 6082-T6, the results are most conservatives.

Table 4: Statistical results of $\chi_{L,ref.}/\chi_{L,F.E.}$ ratio for all cases

Load Cases	Number	Proposal	Mean	C.O.V.	Max.	Min.	< 0.7 [%]	< 0.9 [%]	> 1.10 [%]
All load cases	441	O.I.C.	0.960	0.047	1.125	0.839	0	8	1
		CSA	0.829	0.094	1.017	0.630	5	82	0
N	63	O.I.C.	0.954	0.030	0.990	0.860	0	5	0
		CSA	0.932	0.062	1.017	0.810	0	27	0
M	63	O.I.C.	0.956	0.028	1.023	0.899	0	2	0
		CSA	0.824	0.082	0.966	0.679	3	86	0
$N + M\ (\theta = 15°)$	63	O.I.C.	0.925	0.040	0.989	0.849	0	30	0
		CSA	0.885	0.039	0.948	0.819	0	68	0
$N + M\ (\theta = 30°)$	63	O.I.C.	0.940	0.044	1.013	0.839	0	16	0
		CSA	0.833	0.052	0.929	0.738	0	92	0
$N + M\ (\theta = 45°)$	63	O.I.C.	0.971	0.043	1.078	0.893	0	3	0
		CSA	0.794	0.061	0.902	0.680	3	98	0
$N + M\ (\theta = 60°)$	63	O.I.C.	0.985	0.054	1.125	0.872	0	2	5
		CSA	0.769	0.072	0.895	0.641	10	100	0
$N + M\ (\theta = 75°)$	63	O.I.C.	0.988	0.047	1.124	0.911	0	0	3
		CSA	0.766	0.077	0.885	0.630	16	100	0

As can be remark from Table 4, $\chi_{L,O.I.C.}/\chi_{L,F.E.}$ has average values between 0.94 and 0.99 for all loading cases. Furthermore, the C.O.V. (Coefficient of Variation) for all O.I.C loading cases is less than 0.054. This demonstrates the effectiveness of the O.I.C approach in predicting the strength of aluminum CHS. It can also be argued that all $\chi_{L,O.I.C.}/\chi_{L,F.E.}$ results are between 0.9 and 1.10, proving that O.I.C. is not prone to being conservative or unsafe. The CSA S157, on the other hand, shows highly conservative resultants in the case of combined and bending loads. This confirms the previous observations in Fig. 13 and 15. Finally, the fact that the average $\chi_{L,CSA.}/\chi_{L,F.E.}$ result is below 0.88 for all loading cases, with C.O.V. above 0.05, shows that CSA S157 is less accurate than O.I.C. in predicting the strength of aluminum CHS.

5. Conclusion

This paper investigates the local buckling behavior of short circular hollow section (CHS) extruded aluminum members subjected to combined bending and compression loads through numerical studies. Before conducting a comprehensive parametric study, the numerical model was validated, demonstrating that the numerical model can accurately predict the approximate resistances of CHS within the required range. The parametric study facilitated the implementation of a new design approach based on the Overall Interaction Concept (O.I.C.). A comparison between the O.I.C. predictions and finite element results shows that this new approach effectively predicts the resistances of CHS. It is also less conservative and more accurate than the results provided by the CSA S157 standard.

References

"Aluminum Design Manual 2020 | The Aluminum Association." https://www.aluminum.org/aluminum-design-manual-2020.

Beaulieu, Denis. "Calcul des charpentes d'aluminium."

Beyer, André. 2017. "Résistance Des Barres En Acier à Section Ouverte Soumises à Une Combinaison d'effort Normal, de Flexion et de Torsion." http://www.theses.fr/2017LORR0204/document.

Boissonnade, N, J Nseir, and E Saloumi. 2013. "The Overall Interaction Concept: An Alternative Approach to the Stability and Resistance of Steel Sections and Members."

Canada, Ressources naturelles. 2018. "Faits sur l'aluminium." https://ressources-naturelles.canada.ca/nos-ressources-naturelles/mines-materiaux/donnees-statistiques-et-analyses-sur-lexploitation-miniere/faits-mineraux-metaux/faits-sur-laluminium/20568.

"CSA S157-17/S157.1-17." 2022.

Dahboul, Sahar, Liya Li, Tristan Coderre, and Nicolas Boissonnade. 2023. "O.I.C.-Based Design of Extruded and Welded Aluminum I-Sections." *Structures* 58: 105504. doi:10.1016/j.istruc.2023.105504.

Echeverri Loaiza, Mariana, Pablo Rico Gómez, Liya Li, Carlos Graciano, and Nicolas Boissonnade. 2024. *On the Definition of Geometrical Imperfections in the F.E. Modelling of CHS in Compression*.

"EN1999 Eurocode 9: Design of Aluminium Structures." 2001. *Proceedings of the Institution of Civil Engineers - Civil Engineering*. https://www.icevirtuallibrary.com/doi/10.1680/cien.2001.144.6.61.

Georgantzia, Evangelia, Michaela Gkantou, and George S. Kamaris. 2021. "Aluminium Alloys as Structural Material: A Review of Research." *Engineering Structures* 227: 111372. doi:10.1016/j.engstruct.2020.111372.

Hayeck, Marielle. 2016. "Development of a New Design Method for Steel Hollow Section Members Resistance."

Li, Liya, Sahar Dahboul, Prachi Verma, Pampa Dey, Mario Fafard, and Nicolas Boissonnade. 2023. "An Experimental Study on the Local Instability of Aluminum Circular Hollow Sections." In *Proceedings of the Canadian Society for Civil Engineering Annual Conference 2023, Volume 12*, eds. Serge Desjardins, Gérard J. Poitras, Ashraf El Damatty, and Ahmed Elshaer. Cham: Springer Nature Switzerland, 295–305.

Li, Liya, Sahar Dahboul, Prachi Verma, Pampa Dey, Mario Fafard, and Nicolas Boissonnade. 2023. "O.I.C.-Based Design of Aluminum Circular Hollow Sections under Compression or Pure Bending." *Engineering Proceedings* 43(1): 31. doi:10.3390/engproc2023043031.

Li, Liya, Lucile Gérard, Markus Kettler, and Nicolas Boissonnade. 2022. "The Overall Interaction Concept for the Design of Hot-Rolled and Welded I-Sections under Combined Loading."

Nseir, Joanna. 2015. "Development of a New Design Method for the Cross-Section Capacity of Steel Hollow Sections."

Rong, Bin, Yichun Zhang, Song Zhang, and Zhenyu Li. 2022. "Experiment and Numerical Investigation on the Buckling Behavior of 7A04-T6 Aluminum Alloy Columns under Eccentric Load." *Journal of Building Engineering* 45: 103625. doi:10.1016/j.jobe.2021.103625.

"Stability of Structures." https://www.worldscientific.com/doi/epdf/10.1142/7828.

Zhu, Ji-Hua, and Ben Young. 2006. "Aluminum Alloy Circular Hollow Section Beam-Columns." *Thin-Walled Structures* 44(2): 131–40. doi:10.1016/j.tws.2006.02.006.

Zhu, Ji-Hua, and Ben Young. 2008. "Numerical Investigation and Design of Aluminum Alloy Circular Hollow Section Columns." *Thin-Walled Structures* 46(12): 1437–49. doi:10.1016/j.tws.2008.03.006.